



HAL
open science

Deformation of gas-liquid interfaces in a non-Newtonian fluid at high throughputs inside a microfluidic device and effect of an expansion on bubble breakup mechanisms

Julian Sepulveda, Agnès Montillet, Dominique Della Valle, Catherine Loisel,
Alain Riaublanc

► To cite this version:

Julian Sepulveda, Agnès Montillet, Dominique Della Valle, Catherine Loisel, Alain Riaublanc. Deformation of gas-liquid interfaces in a non-Newtonian fluid at high throughputs inside a microfluidic device and effect of an expansion on bubble breakup mechanisms. *Chemical Engineering Science*, 2020, 213, pp.115377. 10.1016/j.ces.2019.115377 . hal-02479911

HAL Id: hal-02479911

<https://hal.science/hal-02479911>

Submitted on 21 Dec 2021

HAL is a multi-disciplinary open access archive for the deposit and dissemination of scientific research documents, whether they are published or not. The documents may come from teaching and research institutions in France or abroad, or from public or private research centers.

L'archive ouverte pluridisciplinaire **HAL**, est destinée au dépôt et à la diffusion de documents scientifiques de niveau recherche, publiés ou non, émanant des établissements d'enseignement et de recherche français ou étrangers, des laboratoires publics ou privés.



Distributed under a Creative Commons Attribution - NonCommercial 4.0 International License

Deformation of gas-liquid interfaces in a non-Newtonian fluid at high throughputs inside a microfluidic device and effect of an expansion on bubble breakup mechanisms

Julian Sepulveda¹, Agnès Montillet^{1*}, Dominique Della Valle², Catherine Loisel^{2,3}, Alain Riaublanc⁴

¹ LUNAM, Université de Nantes, CNRS, GEPEA, UMR6144, Saint-Nazaire (France).

²ONIRIS, Nantes (France)

³ ONIRIS, GEPEA, UMR CNRS 6144, Nantes (France)

⁴ UR1268 Biopolymères, Interactions, Assemblages, INRA, Nantes (France)

Keywords:

Bubble breakup, Microfluidics, Tip-streaming, Two-phase flow, Foams, Non-Newtonian fluid,

Abstract

This work is focused on the development of a compact continuous process for the production of food foams with controlled properties. Cross shaped channels of infra millimeter size are used and the two-phase flow pattern is analyzed in order to identify the mechanisms of bubble deformation and breakup at very high velocities [$\sim 2\text{-}20\text{ m}\cdot\text{s}^{-1}$]. Two different microchannel designs are used, differing by the presence of an abrupt expansion in one of the devices. Similar breakup mechanisms are observed in both devices in the cross-shaped channels and an additional elongational flow due to the expansion. The expansion was found to intensify bubble breakup. All the experiments are carried out with the same gas content and the same liquid mix prepared from biosourced molecules (xanthan gum and whey proteins). A dimensional analysis is proposed in order to model the diameter of bubbles at the moment of their formation.

1 Introduction

Foams are colloidal dispersions in which a gas is distributed in a continuous phase (Schramm, 2014). The particular structure of these systems makes them highly appreciated for process and product applications in fields such as pharmaceuticals, food industry, cosmetics and firefighting (Campbell et al., 2008; Stevenson, 2012). They are known to impart to products desired characteristics such as lightness, consistency, thermal insulation and mechanical resistance (Cantat et al., 2013). The structural properties of foams, namely gas volume fraction and bubble size distribution govern the end product characteristics (Drenckhan and Saint-Jalmes, 2015; Francis, 2000; Müller-Fischer and Windhab, 2005). Microfluidics has recently appeared as a promising alternative for production of foams and emulsions. This technology concerns the handling of fluid flows with channels of submillimetric dimensions (Stone et al., 2004). The advantages of this technology are enhanced mixing, cheaper manufacturing and reduced operating costs (Afzal and Kim, 2014; Bandara et al., 2015; Kandlikar et al., 2014), but also the production of monodisperse bubbles (Garstecki et al., 2004) and droplets (Link et al. 2004) in creep flow conditions. Therefore, the use of microchannels allows the tailoring of foam textural properties thanks to the remarkable control on the structural properties (Anna, 2016; Laporte et al., 2014).

Emulsion and foam production results in the creation of liquid-liquid and gas-liquid interfaces respectively. It can be described as a process of interface deformation and rupture that allows the creation of new smaller bubbles and droplets. Taylor (1934) was one of the first authors to investigate the deformation of drops in Newtonian fluids under shear and extensional flows in viscous laminar regime. His works were based on the balance between the “breaking” forces (external viscous stress) and the “resisting” forces (Laplace forces) undergone by the droplets. This force balance is expressed by the drop (or bubble) Capillary number (Ca), defined as the ratio of viscous and interfacial forces. Grace’s work (Grace, 1982) extended these results and became the reference for the study of drops breakup. Although that study was originally performed on liquid-liquid dispersed system, it has also been applied to gas-liquid dispersions (Müller-Fischer et al., 2008). When the Reynolds number is much above unity, in the inertial laminar regime, additional inertial forces may contribute to bubble (and drop) breakup (Hessel et al., 2009). They are usually represented by the Weber

* Corresponding author Agnès.Montillet@univ-nantes.fr

number (Anna, 2016; Drenckhan and Saint-Jalmes, 2015). Either Capillary number or Weber number measure the contribution of the external forces on the deformation of the interfaces, depending on the Reynolds number.

Several physical descriptions have been proposed as to how drops and bubbles deform and ultimately break. The main breakup mechanisms described in the literature are tip-streaming (Drenckhan and Saint-Jalmes, 2015; Jain, 2017), binary or capillary breakup (Barthès-Biesel and Acrivos 1973; Janssen et al. 1994), end-pinching (Leal, 2004; Stone, 1994), and ligament fragmentation (Eggers and Villermaux, 2008; Marmottant and Villermaux, 2004; Rayleigh, 1878). These different mechanisms may take place in the foaming processes, depending on the flow geometry, the liquid formulation, and the operating conditions.

The general context of this work is to propose a design enhancing the efficiency of foam production with microsystems. The present study is focused on the case of an abrupt expansion integrated to a reference design that consists of a cross composed of four identical straight channels. The performances of the two systems are compared, based on the observation by high-speed imaging in the outlet channel, as well as on the characteristics of the final product, especially its bubble size distribution. In order to operate in conditions relevant for food industrial applications, high throughputs $10\text{-}20\text{ L}\cdot\text{h}^{-1}$ ($\sim 50\text{-}350\text{ ml}\cdot\text{min}^{-1}$) are implemented. These flowrates are much higher than the range 0 to $1\text{ ml}\cdot\text{min}^{-1}$ commonly found in traditional microfluidic applications (Cubaud & Ho, 2004; Fu & Ma, 2015; Garstecki et al 2004; Haase, 2016) and closer to processing conditions employed with static mixers and rotor-stators (Vial & Djelveh, 2013). The liquid phase is a solution prepared from biosourced ingredients and exhibits a non-Newtonian behavior. For the sake of comparisons, the final void fraction of the foams is set at 0.57 in all the experiments.

2 Materials and Methods

2.1 Experimental setup

The experimental setup which is described in Fig. 1 is designed for foaming production. It was manufactured in the laboratory GEPEA (France). A three-piston pump (Armen instruments) ensures a constant flow of the aqueous solution. Simultaneously, gaseous nitrogen is conveyed from a compressed gas cylinder to the microsystems. Gas flowrate is controlled and measured using a mass flowmeter (EL-FLOW Prestige, Bronkhorst). The gas and the solution are mixed inside the microchannels leading to the genesis of a bubble train. Nitrogen (N_2) is used as the gas phase, as it contributes to the foam stability by being less soluble than other gases (Cantat et al., 2013; Weaire and Hutzler, 1999). The gas-liquid mixture is then conveyed through two successive tubes allowing a progressive pressure relaxation. The first tube (PTFE) has an internal diameter of 0.16 cm and a length of 1 m whereas the second plastic tube has an internal diameter of 1 cm and a length of 5 m . Between the mixing in the microsystem and the outlet of the process, the mixture progressively evolves into the final foam. At the end of the process, the foam goes through a visualization cell to analyze the bubble size distribution of the end product. Pressure sensors (Gems 3100 series) with operating ranges between 0 to 10 bars (relative pressure) are placed before and after the microsystems.

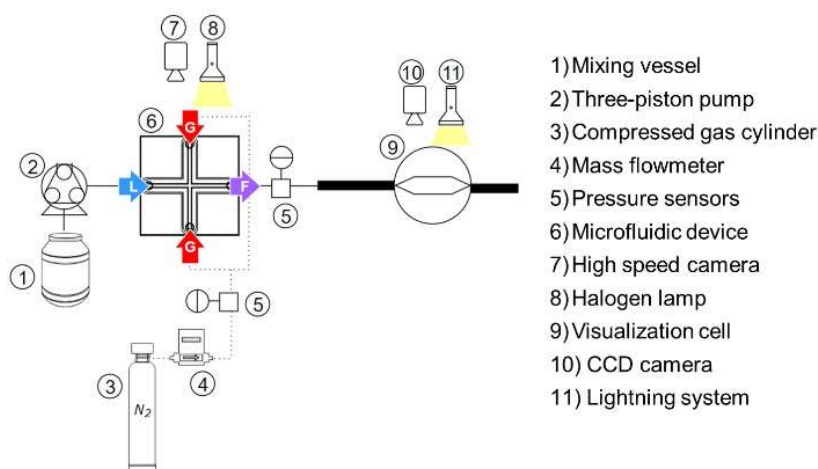


Fig. 1 Schematization of the experimental setup

The two microsystems used are shown in Fig. 2. The first device (CX600) is a cross-flow configuration with four squared channels of section $600 \times 600 \mu\text{m}^2$ and 2 cm length. The modified device (CX-E-600) presents the same cross-shaped design, but also includes an abrupt expansion in the outlet channel. This expansion consists in connecting the mixing channel, having a section $600 \times 600 \mu\text{m}^2$, to a channel having a section $1000 \times 1000 \mu\text{m}^2$. The top sides of the two channels are aligned as these channels are obtained by milling a polymethylmetacrylate (PMMA) plate. Both of them measure 2 cm in length. As explained, one plate of PMMA is carefully milled with a fraise to create the squared microchannels. A groove is also milled around the channels and filled with a joint in order to prevent leakage of fluids. A second PMMA plate is coupled to the first one. The two plates are fixed with screws in order to enable the devices to withstand the high pressures reached with the range of flowrates implemented in this research. As shown in Fig. 2, the liquid (L) is introduced in the device through one of the channels while the gas (G) is injected at an angle of 90° using two channels. The train of bubbles formed (F) then comes out through the remaining channel. A high-speed camera (Highspeedstar 6, La Vision) is used to capture the train of bubbles.

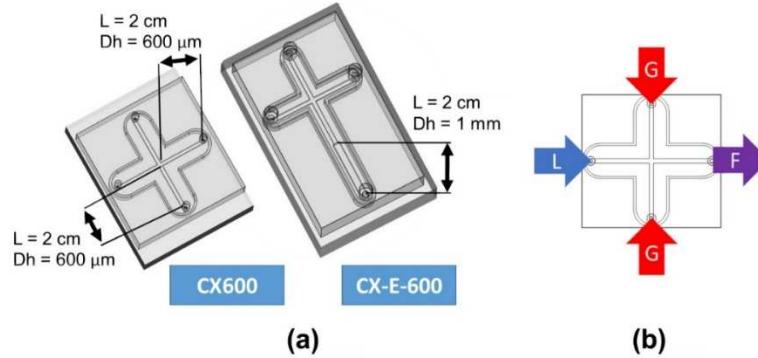


Fig. 2 (a) Microfluidic devices and their characteristic dimensions (length and hydraulic diameter). Cross-flow device (CX600) and cross-flow device with an integrated abrupt expansion (CX-E-600). **(b)** Configuration for the injection of the fluids. Foaming solution (L), gaseous nitrogen (G), foam (F)

2.2 Fluids

2.2.1 Solution preparation

The foaming solution is prepared by mixing whey protein isolate (Pronativ[®] 95 from Lactalis France), xanthan gum (Ketrol[®] AP from Kelco), and demineralized water. The whey protein isolate (WPI) provides the surface-active property necessary to limit foam destabilization. Concentration of WPI was set to 3% (w/w) creating an excess concentration for instantaneous diffusion (Puerta-Gomez, 2014). Xanthan gum (XG) is a thickening agent of industrial relevance (Lieu, 2014), that can be dissolved at room temperature. The use of xanthan aqueous solutions has two major advantages. Firstly, they can act as foam stabilizers (Cantat et al., 2013; Stevenson, 2012) thanks to their large viscosity at rest. Secondly, they exhibit a marked shear thinning behavior with very low apparent viscosity at high shear rates, which in turn facilitates their injection and handling into microchannels at high throughputs. XG concentration was set to 0.4% (w/w), to prevent complexation with WPI (Benichou et al. 2007) while ensuring a sufficiently high concentration that favors foam stabilization. Solutions are prepared at room temperature in a 7 L mixing vessel using an overhead stirrer (RZR 2020 from Heidolph instruments). The pH of solution is fixed at 6.5 and no preservative agent is needed as the solutions are used immediately after preparation.

2.2.2 Rheological behavior

Rheological characterization of aqueous solutions is performed with an AR1000 rheometer (TA instruments) using a cone-plate geometry (40 mm diameter and 4° cone angle). The flow curves are obtained by stress-imposed procedures at 20°C . The viscosity of the solution (μ_L) at the process conditions is then fitted by using a Carreau-Yasuda model (Eq. 1).

$$\frac{\mu_L - \mu_1}{\mu_1 - \mu_2} = \frac{1}{(1 + (\lambda \dot{\gamma})^a)^{m/a}} \quad (1)$$

At the maximal shear rate available with the AR1000 Rheometer, the xanthan gum solution has not yet attained the second Newtonian plateau. A microfluidic rheometer based on visualization of laminar co-flow was then employed for the high shear rates domain $[10^3\text{-}10^5] \text{ s}^{-1}$ (FLUIDICAM^{RHEO}, Formulation Toulouse, FRANCE). Both data sets are plotted in the supplementary material 1 (online) and the fitting parameters are given in table 1.

Table 1. Parameters of the Carreau-Yassuda model for the solution from WPI 3% and XG 0.4%

| WPI3XG04 | | | |
|---|-----------|-----------------------|------|
| 1 st Newtonian plateau viscosity | μ_1 | 146.5 | Pa.s |
| 2 nd Newtonian plateau viscosity | μ_2 | 2.08×10^{-3} | Pa.s |
| Transition parameter | a | 1.12 | - |
| Relaxation time | λ | 34 | s |
| behavior index (n-1) | m | 0.85 | - |

2.2.3 Surface tension

The surface tension of the solutions was characterized using the tensiometer KrüssTM K12 using with the Wilhelmy plate method (Butt et al., 2003). Three temperatures were tested (5, 15, and 25°C) and the equilibrium surface tension at 20°C was found by interpolation (46 mN/m). The use of equilibrium surface tension in microfluidics is common practice when surfactants are present in high amounts (Anna, 2016).

2.3 Flow conditions

The experiments are carried out at room temperature $20^\circ\text{C} \pm 2^\circ\text{C}$. The gas and liquid flowrates investigated (data in supplementary material 2) were selected in order to obtain foams in the dispersed regime having void fractions of 0.57 ± 0.02 :

$$\alpha = \frac{\text{gas volume}}{\text{foam volume}} \quad (2)$$

This value agrees with those generally encountered in food applications (Borwankar and Case, 1997). As for the void fraction inside the channel, it is calculated as follows:

$$\alpha = \frac{U_G}{U_G + U_L} \quad (3)$$

With U_L and U_G being the liquid and gas superficial velocities respectively. The absolute pressure of gas injection P_{abs} (data in supplementary material 2) is used to calculate volumetric gas flowrate Q_{vG} which in turn is used to find the gas superficial velocity that is used in Eq. 3 to find the void fraction in the channel at P_{abs} .

2.4 Visualization, data acquisition and treatment of the bubbles

The bubbles formed in the microfluidic devices were observed using a high-speed camera (HighSpeedStar6 from La vision) with a Precise Eye lens, an adapter tube and extension tubes from Navitar. The image capture was performed at 5000 fps, shutter speed of 10^{-6} s and image resolution of 1024×1024 Pixels². Three zones were visualized: zone A corresponds to the square channel $600 \times 600 \mu\text{m}^2$ where the train of bubbles is formed (see Fig. 3a and 5a). Zone B corresponds to the passage from the channel $600 \times 600 \mu\text{m}^2$ to the abrupt expansion (see Fig. 5a). Finally, the third zone, zone C is located at the end of the expansion channel (see Fig. 5a) where individual bubbles could actually be identified. Images are further processed using the image analysis software ImageJ.

2.5 Measurements of the bubble size distribution inside the microsystem

The bubble size distributions inside the main channel were built up based on a volume equivalent diameter. The bubble volume V_b is estimated considering a cylindrical form, with the maximal radial and axial dimensions of the bubble, B and L respectively, provided by image analysis (Eq. 4). The equivalent diameter is then determined from a spherical

bubble having the same volume (Eq. 5). Finally, the values are converted to atmospheric pressure using Boyle's law (Eq. 6) for later comparison with bubble sizes at the end of the process.

$$V_b = \frac{\pi B^2}{4} L \quad (4)$$

$$V_b = \frac{\pi d_{eq}^3}{6} \quad (5)$$

$$\frac{d}{d_0} = \left(\frac{P_0}{P}\right)^{1/3} \quad (6)$$

2.6 Measurements of the bubble size distribution of the final foams

The size distribution of bubbles at the outlet of the process was evaluated with a CCD camera XCL-5005 with a resolution of 5 M Pixels (Sony, Japan), coupled with the same set of optical attachments described in section 2.4. The bubbles were captured in a planar transparent cell placed just before the end of process and analyzed using ImageJ following a similar procedure to that used for bubble sizes inside the main channel. More than 500 bubbles are analyzed to ensure a representative sample.

3 Results and Discussion

3.1 Validation of the visualizations

Since bubbles travel at very high speeds, it is necessary to carry out an analysis of the adequacy of the camera resolution. In order to validate the conclusions drawn from the images on the bubble shapes and sizes, it is essential to determine that the observed shapes are not due to blur effects. The analysis was performed on the bubbles going through the main channel at bubble velocities of around $20 \text{ m}\cdot\text{s}^{-1}$ ($Q_{vL} = 16.4 \text{ L}\cdot\text{h}^{-1}$ and $Q_{mG} = 31 \text{ g}\cdot\text{h}^{-1}$). The camera shutter speed was $1 \mu\text{s}$. The bubble has traveled a distance (x) of $20 \mu\text{m}$ during photo capture. The bubbles in the channel $600 \times 600 \mu\text{m}^2$ are quite monodisperse presenting average equivalent diameter (d) of $350 \mu\text{m}$. Therefore, the uncertainty of the bubble shape due to the camera characteristics calculated as $(100x/d)$ is equal to 5.7% . This value is sufficiently low to ensure that the measurements of bubble sizes by image analysis are reliable.

3.2 Bubbles morphology and flow typology

3.2.1 Visualizations inside microfluidic device CX600

Visualizations of the bubble formation and typology inside the channel $600 \times 600 \mu\text{m}^2$ for the device CX600 at 4 different flowrates can be seen in Fig. 3b-e. In general, the bubble sizes decrease when the flowrate is increased from b) to e), while greater polydispersity of bubbles size is observed. An increase in the flowrate induces more elongated gas threads at the moment of bubble formation (Muijlwijk et al., 2016) leading to multiple possible pinch-off points which would explain that smaller bubbles and greater polydispersity are obtained for the highest flowrates. The teardrop shapes of the bubbles observed are common for droplets and bubbles travelling through viscoelastic fluids (Tsamopoulos et al., 2008). However, interfacial phenomena are also believed to contribute to the characteristic rearrangements of the bubbles.

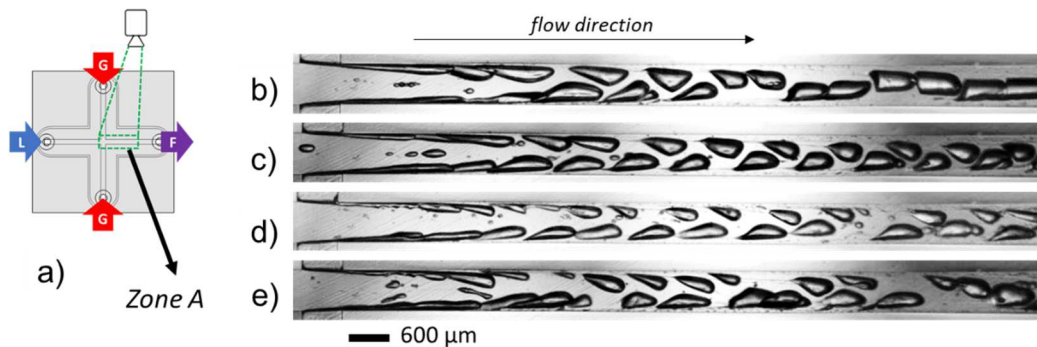


Fig. 3 (a) Visualization at the area of bubble formation (Zone A) in the channel $600 \times 600 \mu\text{m}^2$ of the device CX600. (b)-(e) images at different process conditions: (b) $Q_{vL} = 11 \text{ L}\cdot\text{h}^{-1}$ and $Q_{mG} = 21.6 \text{ g}\cdot\text{h}^{-1}$ (c) $Q_{vL} = 13.7 \text{ L}\cdot\text{h}^{-1}$ and $Q_{mG} = 26.5 \text{ g}\cdot\text{h}^{-1}$ (d) $Q_{vL} = 16.4 \text{ L}\cdot\text{h}^{-1}$ and $Q_{mG} = 31 \text{ g}\cdot\text{h}^{-1}$ (e) $Q_{vL} = 19 \text{ L}\cdot\text{h}^{-1}$ and $Q_{mG} = 36.4 \text{ g}\cdot\text{h}^{-1}$

3.2.2 Mechanisms of bubble formation in the mixing microchannel

Bubble detachment from the gas threads is believed to be a result of pressure forces behind the emerging bubble and shear forces as stated by (Muijlwijk, 2017) for the case of droplet generation in a T-junction device. To identify the type of bubble formation regime, one may refer to the Capillary number of the continuous phase (Eq. 7).

$$Ca_L = \frac{\mu_L U_L}{\sigma} \quad (7)$$

The process viscosity of the liquid phase, μ_L , is computed according to the Carreau-Yasuda model (Eq. 1) at the process shear rate, $\dot{\gamma}_{app}$, given in Eq. 8. The factor 7.115 is calculated according to Comolet (1994) for established flows in rectangular channels.

$$\dot{\gamma}_{app} = 7.115 \frac{U_G + U_L}{D_h} \quad (8)$$

The liquid Capillary numbers of the bubbles flowing through zone A can be found in the supplementary material 2. For liquid flow rates in the range of 11 to 19 L.h⁻¹ in the device CX600, the liquid Capillary numbers fall in the interval 0.4-0.75. According to Anna (2016), in the condition of a Capillary number of the continuous phase higher than 0.1 a bubble is formed in the dripping or jetting regime. These regimes are characterized by bubbles (or drops) that are rather small and do not occupy the whole width of the channel as opposed to the situation observed in the squeezing regime.

To distinguish between dripping and jetting regime in co-flowing bubbling, Gañan-Calvo et al. (2006) have proposed a phase diagram based on the Reynolds and Weber numbers of the continuous phase (Eq. 9 and 10), and the viscosity ratio (Eq. 11). These dimensionless numbers can also be found in the supplementary material 2. Fig. 4 presents the superposition of our measurements over this phase diagram. The solid lines represent limits between dripping and jetting regime for various viscosity ratios. For the flowrates presented in Fig. 3, bubbles are being generated in the jetting regime, characterized by longer gas threads where the two fluids meet. These threads may actually break at multiple points leading to less uniform bubble sizes (Utada et al., 2007; Utada, 2008). This is consistent with our visualizations. As can be seen in the photos, a higher flowrate used in fig 3e has led to more heterogeneous bubble sizes when compared for example to fig 3b corresponding to a lower flowrate. A more precise analysis on the effect of the flowrate on bubble sizes is further discussed later discussed in section 3.4.

$$Re_L = \frac{U_L \rho_L d_h}{\mu_L} \quad (9)$$

$$We_L = \frac{\rho_L U_L^2 d_h}{\mu_L} \quad (10)$$

$$\delta = \frac{\mu_G}{\mu_L} \quad (11)$$

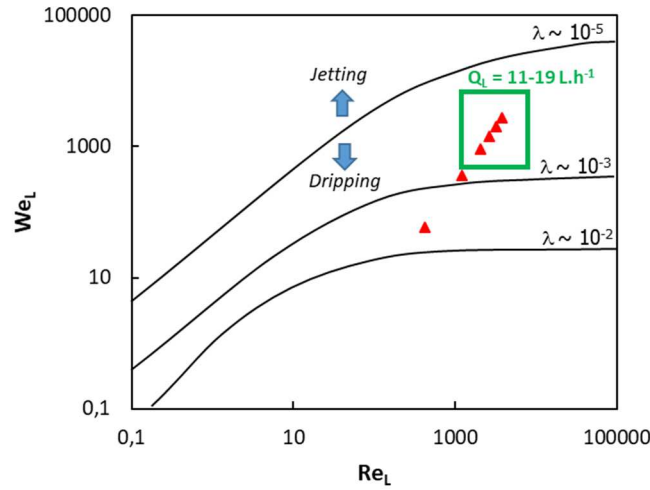


Fig. 4 Phase diagram for transition dripping-jetting regime for different viscosity ratios (Gañan-Calvo et al., 2006). Adapted from (Drenckhan and Saint-Jalmes, 2015). The experimental data located outside the rectangle correspond to experiments carried out at lower flowrates that are not presented in detail in this study.

3.2.3 Visualizations inside microfluidic device CX-E-600

As stated in the methodology section, a second device including an abrupt expansion was also studied (Fig. 5). The Fig. 5a presents the different areas where the visualizations are performed. Some examples of the visualizations for the device CX-E-600 in the three different zones can be seen in Fig. 5b-e. The bubbles in zone A seem slightly different than their counterparts in CX600 (Fig. 3b) for the same flow rate. These bubbles in Fig. 5b do not present the overlapping phenomenon seen for the case of CX600 and appear to be smaller and more isolated. Fig. 6 presents the bubble size distribution in Zone A for both devices at similar process conditions: $Q_{vL} = 11 \text{ L.h}^{-1}$ and $Q_{mG} = 21.6 \text{ g.h}^{-1}$. The CX-E-600 curve presents a wider distribution but smaller bubbles than in the case of CX600. The span ($[D_{90}-D_{10}]/D_{50}$) for the CX-E-600 curve is 0.56 whereas it is 0.34 for CX600. The curves however seem to be alike for bubbles of big sizes. Indeed, the measured D_{90} are respectively $1060 \mu\text{m}$ for CX600 and $1090 \mu\text{m}$ for CX-E-600. The higher number of small bubbles obtained with CX-E-600 explains the wider character of the distribution.

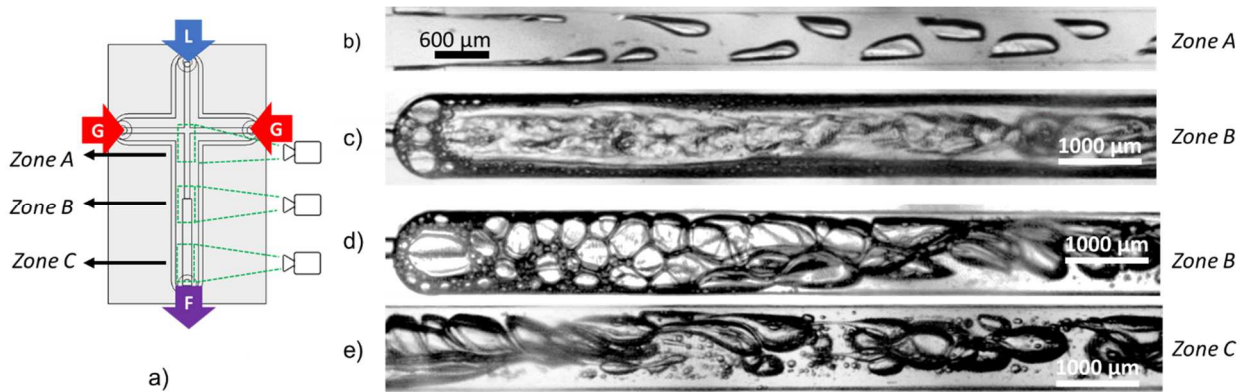


Fig. 5 (a) zones of visualization areas in the device CX-E-600 (b)-(c) visualizations at $Q_{vL} = 11 \text{ L.h}^{-1}$ and $Q_{mG} = 21.6 \text{ g.h}^{-1}$ (b) visualizations in zone A (c) visualization in zone B. (d)-(e) visualizations at a lower flowrate of $Q_{vL} = 3 \text{ L.h}^{-1}$ and $Q_{mG} = 5 \text{ g.h}^{-1}$ to allow proper identification of bubbles in the expansion (d) visualizations in zone B (e) visualizations in zone C

Fig. 5c shows bubbles flowing through the expansion in zone B at $Q_{vL} = 11 \text{ L.h}^{-1}$ and $Q_{mG} = 21.6 \text{ g.h}^{-1}$. Since the expansion has a larger diameter, this increases the fluid thickness through a cross section, making visualization more difficult at the investigated flowrates. Hence, for clear visualization of the phenomena occurring in the expansion, a lower liquid flowrate of $Q_{vL} = 3 \text{ L.h}^{-1}$ is studied. Fig. 5d-e display visualizations in the expansion using a lower flowrate of around $Q_{vL} = 3 \text{ L.h}^{-1}$ and $Q_{mG} = 5 \text{ g.h}^{-1}$ for zones B and C. Bubbles entering zone B expand and their velocity decreases which makes them get closer to each other. The two-phase flow begins to acquire a more foam-like structure. At certain nonsystematic moments, some bubbles get stuck at the entrance of the expansion. They form a bank of air that progressively erodes releasing daughter bubbles. At about 5 mm from the expansion entrance, the visualization of the bubbles becomes easier as we move away from the bank of air. Visualizations were therefore carried out in zone C

in order to identify behavior of individual bubbles. The flow in this appears to be rather chaotic and various bubble morphologies seem to coexist.

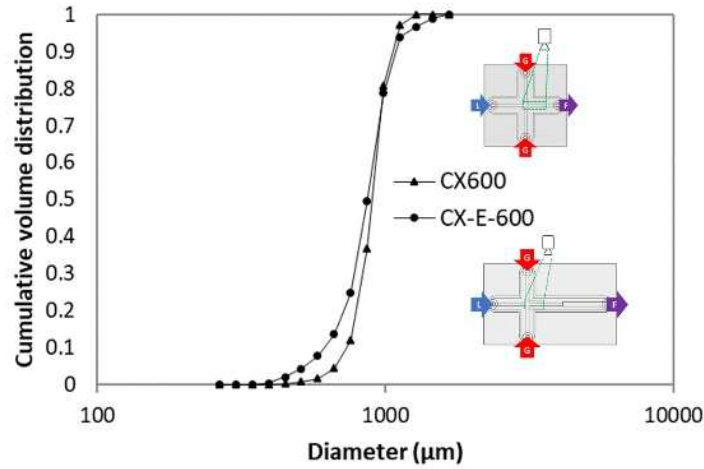


Fig. 6 Comparison of cumulative volume distributions for bubbles formed in zone A for both devices CX600 (triangles) and CX-E-600 (circles) at $Q_{VL} = 11 \text{ L.h}^{-1}$ and $Q_{mG} = 21.6 \text{ g.h}^{-1}$

3.3 Mechanisms of bubble deformation and breakup

3.3.1 Bubbles flowing through the $600 \times 600 \mu\text{m}^2$ channel

A focus on a bubble flowing through the channel $600 \times 600 \mu\text{m}^2$ is presented in Fig. 7. A small elongated tail can be noticed at the downstream extremity of the bubble. Such characteristic tail has been found to be part of a bubble being eroded releasing a train of tiny satellite bubbles (De Bruijn, 1993; Jeong et al., 2012; Moyle et al., 2012). This systematic emission of minute bubbles is said to be a mechanism of bubble breakup known as tip-streaming and only possible in the presence of interfacial tension gradients (De Bruijn, 1989; De Bruijn, 1993). Surface active compounds actually makes the interface more flexible facilitating its deformation and final rupture.

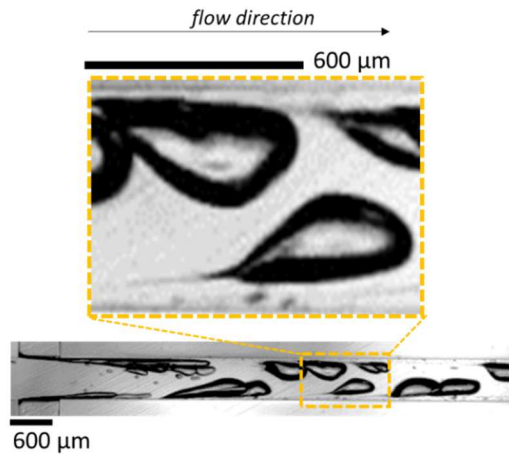


Fig. 7 Zoomed bubble inside the channel $600 \times 600 \mu\text{m}^2$ of the device CX600 at $Q_{VL} = 11 \text{ L.h}^{-1}$ and $Q_{mG} = 21.6 \text{ g.h}^{-1}$

Since interfacial tension gradients have been said to be necessary for tip streaming, it is believed that the interfaces formed in our experiments are not completely saturated, despite the excess of WPI employed. Walstra (2003) has proposed an estimation for the complete adsorption time of surface-active molecules for air-water and oil-water interfaces assuming diffusion-driven adsorption. This adsorption time can be estimated according to Eq. 12. Where t_{ads} corresponds to the time needed for complete adsorption, D is the diffusion coefficient of the surfactant in the solution, c the surfactant or molecule concentration and Γ_{∞} is the surface coverage.

$$t_{ads} \approx 10 \frac{\Gamma_{\infty}^2}{c^2 D} \quad (12)$$

Since β -lactoglobuline is the predominant molecule in whey protein isolates (WPI) a surface coverage of $2.1 \text{ mg}\cdot\text{m}^{-2}$ (Pérez-Fuentes et al., 2017) has been used. A diffusion coefficient of $2.4 \times 10^{-11} \text{ m}^2\cdot\text{s}^{-1}$ has been identified by (Sadek et al., 2015) for WPI. The concentration of WPI in our solutions is 3% w/w which is approximately $30 \times 10^6 \text{ mg}\cdot\text{m}^{-3}$. The adsorption time predicted is therefore 2 ms. The interframe time, the time between photos, is 0.2 ms in our experimental conditions. When two successive photos are compared, it has been possible to confirm that several new bubbles have appeared during the interframe time. Thus, the air-water interfaces are being generated in less than 0.2 ms. The value of t_{ads} being 2 ms is therefore higher than the time of interfacial formation. This means that the interface might not be fully saturated when the bubbles are visualized in the microchannel.

The time of adsorption can actually be lower than the estimated value of 2 ms in convective transport (Walstra, 2003). Since the Reynolds number calculated for our conditions are in the range 2000-4000 (supplementary material 2), inertial effects are significant. Hence, adsorption times under our experimental conditions might be lower than the one calculated for diffusion-driven adsorption. In this case, the adsorption time might be theoretically short enough to fully cover the interface at the timescales of the interface formation. However, there are other factors that will slow down the adsorption of molecules irrespective of diffusion-driven or convective transport.

Polymer adsorption also implies rearrangements in the interface for them to be completely functional (Berton-Carabin et al., 2018). According to (Walstra, 2003), globular proteins might require up to 10^3 s to complete their conformational changes at the interface. This means that even though the adsorption time in convective transport might be lower than 0.2 ms, conformational changes of polymers in the interface require timescales much larger than 0.2 ms. Additionally, complete surface coverage is slowed down by continuous desorption and re-adsorption processes characteristics of polymers (Walstra 2003). Finally, a third factor that might also affect kinetics of surface coverage in our experiments is the presence of the molecules of xanthan gum in our solutions. The concentration of this hydrocolloid in our solutions is 0.4% w/w that according to (Wyatt et al., 2011) would imply a concentrated regime. Under this condition, the xanthan gum molecules might cause steric hindrance reducing proteins mobility towards the interface. In our opinion, the presence of xanthan in our solutions is a key factor in the evolution of molecules of proteins towards the created interface.

The flow characteristics are also believed to play a key role in the establishment of tip streaming. The viscous forces close to the channel walls are probably leading to important stresses shearing the bubble tip and thus leading to interfacial transport of the surface-active molecules which ultimately favors the establishment of concentration gradients. The tip of the bubble now being more fully covered with proteins will be more easily eroded under the viscous stresses characteristic of near-wall flows.

3.3.2 Bubbles flowing through abrupt expansion

In the expansion ($1000 \times 1000 \mu\text{m}^2$), bubbles have been observed to deform by stretching (Fig. 5e). However, the deformations do not follow any pattern and appear to be rather chaotic. Swirling flows have already been pointed out in abrupt expansions (Hallett and Günther, 1984; Mak and Balabani, 2007). This in turn creates stagnation zones that develop elongational flows. Fig. 8 presents the case of a single bubble undergoing deformation and rupture in the expansion at $Q_{VL} = 3 \text{ L}\cdot\text{h}^{-1}$. These drastic deformations and breakups are taking place at very low liquid Reynolds number of around 126 (data in supplementary material 3). The bubble seems to stretch out and a filament begins to develop. Finally, the thin filament collapses by a necking process resulting in two distinctive bubbles by a mechanism of binary breakup. As opposed to tip-streaming, the binary breakup observed produces bigger bubbles known as daughter bubbles that detach from the parent bubble and are produced more intermittently. The binary breakup mechanism is believed to be related to higher surfactant coverage. Indeed, in the expansion channel, residence time are higher and therefore surfactants would have more time, in the flow conditions, to diffuse and adsorb to the interface.

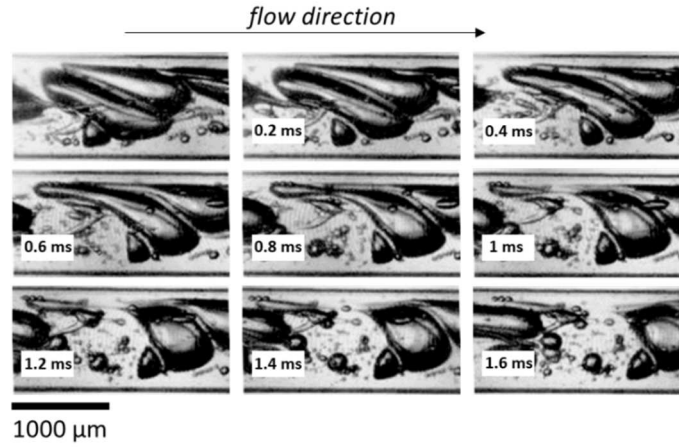


Fig. 8 Bubble breakup visualized in the expansion channel at $Q_{VL} = 3 \text{ L}\cdot\text{h}^{-1}$ and $Q_{MG} = 5 \text{ g}\cdot\text{h}^{-1}$. The interframe time (Δt) is 0.2 ms.

3.3.3 Characterizing bubble breakup

The Taylor-Grace theory (Grace, 1982) provides a critical value of the bubble Capillary number, Ca_{bubble} , allowing the determination of the maximum diameter that can withstand a given stress in specific conditions. It is presented in a famous universal curve, expressed as a function of the viscosity ratio.

$$Ca_{bubble} = \frac{\mu_L \dot{\gamma} d_{eq}}{2\sigma} \quad (13)$$

The bubble Capillary number (Ca_{bubble}) is calculated according to Eq. 13 for a few bubbles observed in the channel $600 \times 600 \mu\text{m}^2$ (zone A) for both devices at liquid flowrates $Q_{VL} = 11 \text{ L}\cdot\text{h}^{-1}$ and $Q_{VL} = 16.4 \text{ L}\cdot\text{h}^{-1}$. Ca_{bubble} for bubbles flowing through expansion (zone C) is calculated at a liquid flowrate of $3 \text{ L}\cdot\text{h}^{-1}$. The results are plotted onto the Grace-curve presented in Fig. 9. Data corresponding to bubbles observed in zone A (circles) are just above the limit line characterizing drop breakup by shear (solid line). In our study, these bubbles were not observed to undergo breakup into two bubbles as described by Grace (1982). However, they presented tip-streaming mechanism (Fig. 7). Grace (1982) also proposed a limit line for the establishment of tip streaming in the presence of surfactants (dotted line). By analyzing this case, it becomes evident that the data points are now significantly above this line. This result is in agreement with our visualizations of Fig. 7.

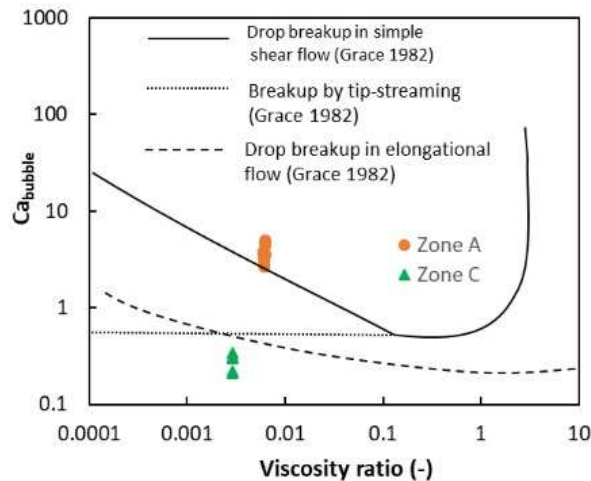


Fig. 9 Superposition on the curves of Grace (1982) for data points corresponding to visualized bubbles in the channel $600 \times 600 \mu\text{m}^2$ (zone A) and in the expansion (zone C)

Concerning data corresponding to bubbles observed in zone C, they have been observed to break into two bubbles in local due to local elongational flows. When plotted onto the Grace curve (triangles), they appear to be under the line for breakup in elongational flow (dashed line). However, visual analysis has provided evidence of bubble rupture linked to

drastic bubble elongations (Fig. 8). Therefore, the Grace curve does not seem to adequately predict breakup of bubbles in a viscoelastic fluid matrix using microsystems at the high throughputs evaluated.

Since the elongated bubbles in the expansion present long filaments, an alternative approach based on [Driessen \(2013\)](#) is proposed. For this purpose, a bubble aspect ratio (Eq. 14) is plotted versus the Ohnesorge number (Eq. 15), a dimensionless number which represents the interplay between viscous, inertial and interfacial forces used in describing rupture of filaments ([Driessen, 2013](#); [Eggers & Villermaux, 2008](#); [Van Hoeve, 2011](#)). With R_0 being the radius of the elongated filament, that is $B/2$.

$$\Gamma = \frac{L}{B} \quad (14)$$

$$Oh = \frac{\mu_L}{\sqrt{\rho_L \sigma R_0}} \quad (15)$$

Fig. 10a presents an example of a bubble located in zone C of the expansion channel developing a gas filament by elongation of the interface at $Q_{VL} = 3 \text{ L.h}^{-1}$. The bubble and the growing filament are schematized in Fig. 10b. The axial (L) and radial (B) dimensions of the filament are measured by image analysis in order to calculate the 2D aspect ratio (Γ). Several successive photos of a single bubble are studied to evaluate the evolution of the filament elongation in terms of the Ohnesorge number and aspect ratio.

Fig. 10c Presents the diagram found in [Driessen \(2013\)](#) for description of liquid filament rupture. The dashed-dotted line corresponds to the linear theory from [Rayleigh \(1878\)](#) establishing the critical aspect ratio above which filament rupture takes place. Three bubbles have been selected to evaluate if this analysis might be extended to the strong elongations and filament detachment observed for the bubbles flowing through the expansion channel. Each bubble is identified with a different marker (square, circle, and triangle). For each marker, each data point presented in the graph corresponds to one photo analyzed.

One photo for each bubble analyzed has been included. The photo selected for each case corresponds to the moment of maximum filament elongation before breaking up or recovering its shape. The data overlaid onto the graph agrees with the phenomena visualized in the photos. This means that the points located above the dash-dotted line correspond exactly to photos where bubbles were the filament detaches itself from the main bubble (circle and square) while the bubble that recovers its shape (triangle) corresponds to symbols that are located below the limit line. These results seem to suggest that the linear theory used in liquid threads ([Castrejon-Pita et al., 2012](#); [Driessen, 2013](#)) might apply for the description of rupture of the gas filaments generated in the expansion. However, additional research studies using different conditions are required to consolidate these suggestions.

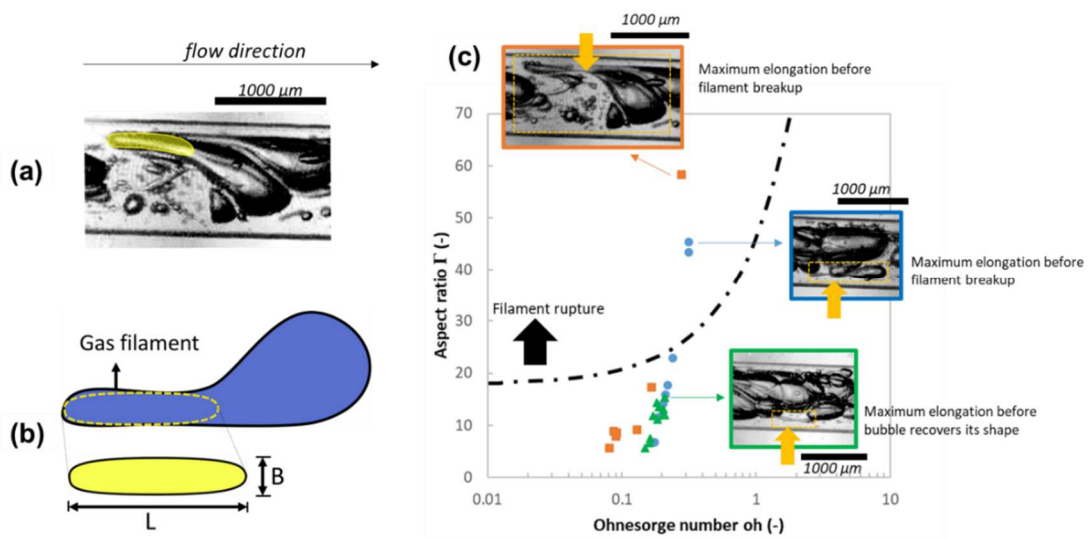


Fig. 10 (a) Photo of an elongated bubble in zone C at $Q_{VL} = 3 \text{ L.h}^{-1}$ (b) schematization of an elongated bubble and characteristic dimensions of the gas filament bubble and the gas filament highlighted in yellow (c) Aspect ratio versus Ohnesorge number for three cases of bubbles (square, circle, and triangle) visualized inside the expansion channel. Markers of the same kind correspond to different sequential images of a same bubble. The dashed-dotted line represents the linear theory defining a critical aspect ratio for filament breakup.

To summarize, different cases of bubble deformation and breakup have been observed in this study (Fig. 11). Inside the channel $600 \times 600 \mu\text{m}^2$, the tip-streaming mechanism was present. Stronger resolutions are needed to access length scales of the satellite bubbles detached from the main bubble. In the expansion, swirling and backwards flows were distinguished. These secondary flows create the appropriate conditions for local elongational flows. Most of the elongated bubbles underwent binary breakup. In fact, elongational flows have already been described as more effective conditions for disrupting droplets (Grace, 1982).

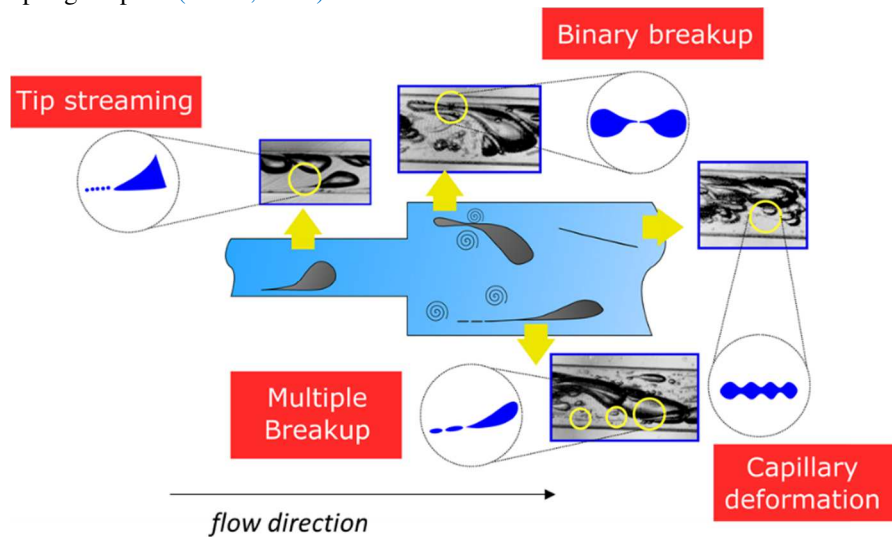


Fig. 11 schematic representation of the observed deformation and breakup mechanisms in microchannels at high throughputs

3.4 Bubble size distribution for bubbles in the microchannels (in-line) and in the end product (off-line)

3.4.1 Bubble sizes in channel $600 \times 600 \mu\text{m}^2$ (Zone A)

Fig. 12 shows the size distribution for bubbles flowing through the channel $600 \times 600 \mu\text{m}^2$ for the device CX600. Two modal values can be identified in each curve. As soon as the flowrates increase, the modal value for big particles decreases while favoring the appearance of smaller bubbles. This increase of flowrates also leads to more polydisperse distributions. In fact, the calculated span for the liquid flowrates 11, 13.7, 16.4, and 19 $\text{L}\cdot\text{h}^{-1}$ were 0.37, 0.56, 0.65, and 0.66 respectively. This confirms the effect of flowrate on bubble size polydispersity already mentioned by Gaillard (2016) for a millifluidic application.

A comparison for the bubbles size distribution in zone A for CX600 vs CX-E-600 was previously presented in Fig. 6 for $Q_{\text{vL}} = 11 \text{ L}\cdot\text{h}^{-1}$ and $Q_{\text{mG}} = 21.6 \text{ g}\cdot\text{h}^{-1}$. The outlines of the curves are very similar, however there is a higher concentration of smaller bubbles for CX-E-600. Those differences might stem from higher pressure drops found for the device CX-E-600 as shown in the supplementary material 2.

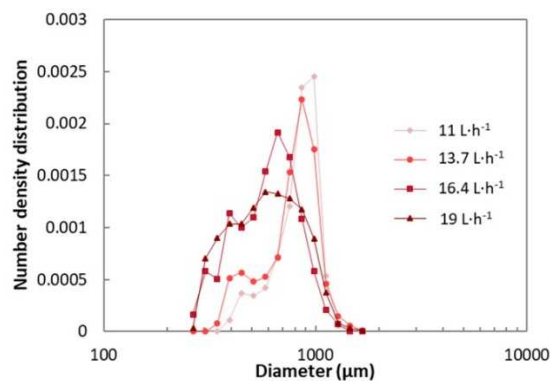


Fig. 12 Effect of the flowrate on the bubbles size distribution for bubbles travelling across zone A for the device CX600

3.4.2 Comparison of in-line and off-line size distributions

Fig. 13 displays the size distribution of the bubbles going through zone A or in-line bubbles (solid lines) along with those at the end of the process or off-line bubbles (dashed lines) for $Q_{\text{vL}} = 11 \text{ L}\cdot\text{h}^{-1}$. Marked differences in the evolution

of granulometry are revealed when the devices CX600 and CX-E-600 are compared. The in-line bubbles for both devices present similar profiles but evolve into two very different distributions for the off-line bubbles. The only difference between CX600 and CX-E-600 is the presence of an abrupt expansion. As mentioned before, this expansion allowed the establishment of extensional flows that led to enhanced bubble deformation and breakup. These results suggest that a slight change in the geometrical configuration of a microsystem might greatly affect end-product structural properties. This highlights the importance of geometrical considerations in the conception of a foaming process system.

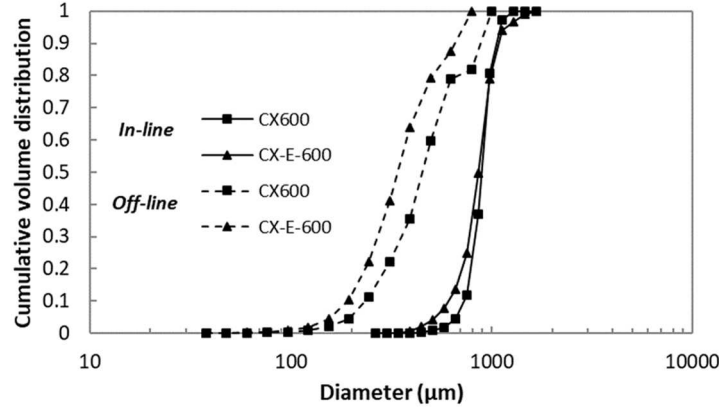


Fig. 13 Cumulative volume distribution for bubbles in zone A or in-line bubbles (solid lines) and bubble sizes at the end of the process or off-line bubbles (dashed line) for both devices CX600 (squares) and CX-E-600 (triangles) at $Q_{vL} = 11 \text{ L.h}^{-1}$ and $Q_{mG} = 21.6 \text{ g.h}^{-1}$

3.5 Modelling bubble sizes in channel $600 \times 600 \mu\text{m}^2$

An attempt to model the bubble Sauter diameter (d_{32}) for bubbles in Zone A (in-line bubbles) by dimensional analysis is proposed. The dimensional analysis was proposed since according to (Çengel and Cimbala, 2014), the best approach to determine flow characteristics where inertial forces are relevant is “to identify the key variables and functional forms using dimensional analysis and then to use experimental data to determine the numerical values of any constants”.

In order to carry out the dimensional analysis a preliminary step of identifying relevant physical variables affecting the process is required. These variables must be physically independent. The Sauter diameter (variable of interest) is expressed as a function of the other variables as shown in Eq. 16:

$$d_{32} = f(U_L, U_G, \rho_L, \rho_G, \mu_L, \mu_G, \sigma, \Delta P, D_h) \quad (16)$$

According to the Vaschy-Buckingham theorem, the target variable d_{32} can be described by a group of dimensionless numbers relating the relevant physical variables (Delaplace et al., 2015; Ruzicka, 2008). After obtaining of all the relevant dimensionless numbers, they are rearranged in order to make appear dimensionless numbers whose physical meanings are already understood (for example Reynolds number) or that are commonly found in a field of study (flowrates ratio in the case of microfluidics). The procedure applied is based on the works of (Delaplace et al., 2015) and (Mary et al., 2013)

The model equation obtained that describes the sizes of the in-line bubbles (zone A) under the experimental conditions is presented in Eq. 17. The coefficients of this monomial expression were calculated by minimizing the sum of the squares of the errors between experimental and predicted values. The mean relative deviation obtained was 3.40% which is a low value ensuring a good prediction.

$$\frac{d_{32}}{D_h} = 21 \left(\frac{Q_G}{Q_L} \right)^{0.29} Re_L^{-0.27} Ca_L^{0.36} \quad (17)$$

Fig. 14 displays the fitting of the empirical model to the experimental data. The model can therefore be considered as an acceptable approximation for the description of the bubble sizes just after their formation in channel $600 \times 600 \mu\text{m}^2$. An analysis of this Equation. shows the importance of the viscous-interfacial forces balance represented by the large exponent of the Capillary number compared to the others. This is consistent with the literature on bubbles in miniaturized channels where Capillary numbers are said to be of key importance in description of phenomena at these

scales (Pipe and McKinley, 2009; Weaire and Drenckhan, 2008). The flowrate ratio and Reynolds number also present relatively large exponents revealing a considerable contribution of the inertial forces to the description of the bubble sizes under the experimental conditions studied. These considerations highlight the importance of accounting for inertial forces (as opposed to classical microfluidics) for the scale-up of microchannel applications to conditions closer to food industrial applications at high flowrates.

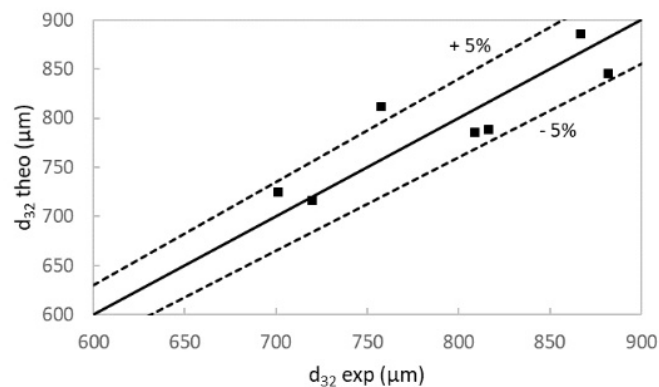


Fig. 14 Modelling of bubble sizes in zone A for both devices CX600 and CX-E-600

4 Conclusion

This study was focused on the investigation of the deformation and breakup mechanisms in a microfluidic system when using high flowrates for a foaming application. Different breakup mechanisms were identified such as tip-streaming, or binary break-up. Their incidence is depending on microchannel geometry. In order to gain more relevant knowledge into the tip-streaming mechanism, images with higher resolution are needed to access the submicrometric length scales characteristic of the satellite bubbles generated. However, the presence of this mechanism may be attested by the visualization of the developed elongated tails and is consistent with the Grace curve analysis. The studied method based on the Ohnesorge number, commonly used for deformation of long liquid filaments, provides good approximation for rupture of bubbles under elongational flows. However, further research should be undertaken for the elaboration of descriptive diagrams specific to foams that consider experimental conditions relevant for industrial applications such as collective effects due to the presence of multiple bubbles and the use of polymer-based foaming solutions. Despite its exploratory nature, this study offers some insight into the possible mechanisms of bubble deformation and breakup in a non-Newtonian liquid matrix inside microchannels at high throughputs. In addition, the importance of the microchannel geometry under such conditions is outlined: foams with smaller bubble size are obtained with the abrupt expansion configuration. This might be of industrial relevance in the tailoring of textural properties of stable foams.

Acknowledgements

This work was carried out with the financial support of the regional programme "Food for Tomorrow / Cap Aliment; Research, Education and Innovation in Pays de la Loire", which is supported by the French Region Pays de la Loire and the European Regional Development Fund (FEDER). We would like to especially thank two members of the technical team of the GEPEA laboratory, Christophe COUDEL and Jean-Luc HAUSER, for the help provided during the development of the experimental setup.

References

- Afzal, A., Kim, K.-Y., 2014. Flow and mixing analysis of non-Newtonian fluids in straight and serpentine microchannels. *Chemical Engineering Science* 116, 263–274. <https://doi.org/10.1016/j.ces.2014.05.021>
- Anna, S.L., 2016. Droplets and Bubbles in Microfluidic Devices. *Annual Review of Fluid Mechanics* 48, 285–309. <https://doi.org/10.1146/annurev-fluid-122414-034425>
- Bandara, T., Nguyen, N.-T., Rosengarten, G., 2015. Slug flow heat transfer without phase change in microchannels: A review. *Chemical Engineering Science* 126, 283–295. <https://doi.org/10.1016/j.ces.2014.12.007>
- Barthès-Biesel, D., Acrivos, A., 1973. Deformation and burst of a liquid droplet freely suspended in a linear shear field. *Journal of Fluid Mechanics* 61, 1. <https://doi.org/10.1017/S0022112073000534>
- Benichou, A., Aserin, A., Lutz, R., Garti, N., 2007. Formation and characterization of amphiphilic conjugates of whey protein isolate (WPI)/xanthan to improve surface activity. *Food Hydrocolloids* 21, 379–391. <https://doi.org/10.1016/j.foodhyd.2006.04.013>

- Berton-Carabin, C.C., Sagis, L., Schroën, K., 2018. Formation, Structure, and Functionality of Interfacial Layers in Food Emulsions. *Annual Review of Food Science and Technology* 9, 551–587. <https://doi.org/10.1146/annurev-food-030117-012405>
- Borwankar, R.P., Case, S.E., 1997. Rheology of emulsions, foams and gels. *Current Opinion in Colloid & Interface Science* 2, 584–589. [https://doi.org/10.1016/S1359-0294\(97\)80049-0](https://doi.org/10.1016/S1359-0294(97)80049-0)
- Butt, H.-J., Graf, K., Kappl, M., 2003. *Physics and Chemistry of Interfaces*. Wiley-VCH Verlag GmbH & Co. KGaA, Weinheim, FRG. <https://doi.org/10.1002/3527602313>
- Campbell, G.M., Scanlon, M.G., Pyle, D.L. (Eds.), 2008. *Bubbles in food. 2: Novelty, health and luxury*. Egan Press, St. Paul, Minnesota, USA.
- Cantat, I., Cohen-Addad, S., Elias, F., Graner, F., Höhler, R., Pitois, O., Rouyer, F., Saint-Jalmes, A., Flatman, R., Cox, S.J. (Eds.), 2013. *Foams: structure and dynamics*, 1. ed. ed. Oxford Univ. Press, Oxford.
- Castrejón-Pita, A.A., Castrejón-Pita, J.R., Hutchings, I.M., 2012. Breakup of Liquid Filaments. *Physical Review Letters* 108. <https://doi.org/10.1103/PhysRevLett.108.074506>
- Çengel, Y.A., Cimbala, J.M., 2014. *Fluid mechanics: fundamentals and applications*, Third edition. ed. McGraw Hill, New York.
- Comolet, R., 1994. *Mécanique expérimentale des fluides. Dynamique des fluides réels, turbomachines*. Masson, Paris.
- Cubaud, T., Ho, C.-M., 2004. Transport of bubbles in square microchannels. *Physics of Fluids* 16, 4575–4585. <https://doi.org/10.1063/1.1813871>
- De Bruijn, R., 1989. *Deformation and breakup of drops in simple shear flows (Thesis)*. Technische Universiteit Eindhoven. <https://doi.org/10.6100/IR318702>
- De Bruijn, R.A., 1993. Tipstreaming of drops in simple shear flows. *Chemical Engineering Science* 48, 277–284. [https://doi.org/10.1016/0009-2509\(93\)80015-1](https://doi.org/10.1016/0009-2509(93)80015-1)
- Delaplace, G., Loubière, K., Ducept, F., Jeantet, R., 2015. *Dimensional Analysis of Food Process*. Elsevier Science & ISTE Press, Oxford, UK.
- Drenckhan, W., Saint-Jalmes, A., 2015. The science of foaming. *Advances in Colloid and Interface Science* 222, 228–259. <https://doi.org/10.1016/j.cis.2015.04.001>
- Driessen, T., Jeurissen, R., Wijshoff, H., Toschi, F., Lohse, D., 2013. Stability of viscous long liquid filaments. *Physics of Fluids* 25, 062109. <https://doi.org/10.1063/1.4811849>
- Eggers, J., Villermaux, E., 2008. Physics of liquid jets. *Reports on Progress in Physics* 71, 036601. <https://doi.org/10.1088/0034-4885/71/3/036601>
- Francis, F.J. (Ed.), 2000. *Encyclopedia of food science and technology*, 2., [rev.] ed. ed. Wiley, New York.
- Fu, T., Ma, Y., 2015. Bubble formation and breakup dynamics in microfluidic devices: A review. *Chemical Engineering Science* 135, 343–372. <https://doi.org/10.1016/j.ces.2015.02.016>
- Gaillard, T., 2016. *Ecoulements confinés à haut et bas Reynolds : génération millifluidique de mousse et drainage de films minces de copolymères (Thesis)*. Université Paris Saclay.
- Gañán-Calvo, A.M., Herrada, M.A., Garstecki, P., 2006. Bubbling in Unbounded Coflowing Liquids. *Physical Review Letters* 96. <https://doi.org/10.1103/PhysRevLett.96.124504>
- Garstecki, P., Gitlin, I., DiLuzio, W., Whitesides, G.M., Kumacheva, E., Stone, H.A., 2004. Formation of monodisperse bubbles in a microfluidic flow-focusing device. *Applied Physics Letters* 85, 2649–2651. <https://doi.org/10.1063/1.1796526>
- Grace, H.P., 1982. Dispersion phenomena in high viscosity immiscible fluid systems and application of static mixers as dispersion devices in such systems. *Chemical Engineering Communications* 14, 225–277. <https://doi.org/10.1080/00986448208911047>
- Hallett, W.L.H., Günther, R., 1984. Flow and mixing in swirling flow in a sudden expansion. *The Canadian Journal of Chemical Engineering* 62, 149–155. <https://doi.org/10.1002/cjce.5450620123>
- Haase, S., 2016. Characterisation of gas-liquid two-phase flow in minichannels with co-flowing fluid injection inside the channel, part I: unified mapping of flow regimes. *International Journal of Multiphase Flow* 87, 197–211. <https://doi.org/10.1016/j.ijmultiphaseflow.2016.08.003>
- Hessel, V., Renken, A., Scouten, J.C., Yoshida, J. (Eds.), 2009. *Micro process engineering: a comprehensive handbook*. Wiley-VCH, Weinheim.
- Jain, S.S., 2017. Flow-induced breakup of drops and bubbles. arXiv:1701.06157 [physics].
- Janssen, J.J.M., Boon, A., Agterof, W.G.M., 1994. Influence of dynamic interfacial properties on droplet breakup in simple shear flow. *AIChE Journal* 40, 1929–1939. <https://doi.org/10.1002/aic.690401202>
- Jeong, W.-C., Lim, J.-M., Choi, J.-H., Kim, J.-H., Lee, Y.-J., Kim, S.-H., Lee, G., Kim, J.-D., Yi, G.-R., Yang, S.-M., 2012. Controlled generation of submicron emulsion droplets via highly stable tip-streaming mode in microfluidic devices. *Lab on a Chip* 12, 1446. <https://doi.org/10.1039/c2lc00018k>
- Kandlikar, S.G., Garimella, S., Li, D., Colin, S., King, M.R., 2014. *heat transfer and fluid flow in minichannels and microchannels.pdf*. Butterworth-Heinemann, Oxford, UK.
- Kockmann, N., 2008. *Transport phenomena in micro process engineering, Heat and mass transfer*. Springer, Berlin ; New York.
- Laporte, M., Loisel, C., Della Valle, D., Riaublanc, A., Montillet, A., 2014. Flow process conditions to control the void fraction of food foams in static mixers. *Journal of Food Engineering* 128, 119–126. <https://doi.org/10.1016/j.jfoodeng.2013.12.017>

- Leal, L.G., 2004. Flow induced coalescence of drops in a viscous fluid. *Physics of Fluids* 16, 1833–1851. <https://doi.org/10.1063/1.1701892>
- Lieu, B.K., 2014. Dynamics and Control of Newtonian and Viscoelastic Fluids (Thesis). University of Minnesota, USA.
- Link, D.R., Anna, S.L., Weitz, D.A., Stone, H.A., 2004. Geometrically Mediated Breakup of Drops in Microfluidic Devices. *Physical Review Letters* 92. <https://doi.org/10.1103/PhysRevLett.92.054503>
- Mak, H., Balabani, S., 2007. Near field characteristics of swirling flow past a sudden expansion. *Chemical Engineering Science* 62, 6726–6746. <https://doi.org/10.1016/j.ces.2007.07.009>
- Marmottant, P., Villermaux, E., 2004. Fragmentation of stretched liquid ligaments. *Physics of Fluids* 16, 2732–2741. <https://doi.org/10.1063/1.1756030>
- Mary, G., Mezdoor, S., Delaplace, G., Lauhon, R., Cuvelier, G., Ducept, F., 2013. Modelling of the continuous foaming operation by dimensional analysis. *Chemical Engineering Research and Design* 91, 2579–2586. <https://doi.org/10.1016/j.cherd.2013.05.020>
- McClements, D.J., 2005. Food emulsions: principles, practices, and techniques, 2. ed. ed, CRC series in contemporary food science. CRC Press, Boca Raton, Fla.
- Moyle, T.M., Walker, L.M., Anna, S.L., 2012. Predicting conditions for microscale surfactant mediated tipstreaming. *Physics of Fluids* 24, 082110. <https://doi.org/10.1063/1.4746253>
- Muijllwijk, K., 2017. Microfluidic methods to study emulsion formation (Thesis). Wageningen University.
- Muijllwijk, K., Berton-Carabin, C., Schroën, K., 2016. Cross-flow microfluidic emulsification from a food perspective. *Trends in Food Science & Technology* 49, 51–63. <https://doi.org/10.1016/j.tifs.2016.01.004>
- Müller-Fischer, N., Tobler, P., Dressler, M., Fischer, P., Windhab, E.J., 2008. Single bubble deformation and breakup in simple shear flow. *Experiments in Fluids* 45, 917–926. <https://doi.org/10.1007/s00348-008-0509-1>
- Müller-Fischer, N., Windhab, E.J., 2005. Influence of process parameters on microstructure of food foam whipped in a rotor–stator device within a wide static pressure range. *Colloids and Surfaces A: Physicochemical and Engineering Aspects* 263, 353–362. <https://doi.org/10.1016/j.colsurfa.2004.12.057>
- Pérez-Fuentes, L., Drummond, C., Farauto, J., Bastos-González, D., 2017. Adsorption of Milk Proteins (β -Casein and β -Lactoglobulin) and BSA onto Hydrophobic Surfaces. *Materials* 10, 893. <https://doi.org/10.3390/ma10080893>
- Pipe, C.J., McKinley, G.H., 2009. Microfluidic rheometry. *Mechanics Research Communications* 36, 110–120. <https://doi.org/10.1016/j.mechrescom.2008.08.009>
- Puerta-Gomez, A.F., 2014. Characterization of biopolymers for use as matrices for encapsulation of hydrophobic compounds (Thesis). Texas A&M University, Texas, USA.
- Rayleigh, Lord, 1878. On The Instability Of Jets. *Proceedings of the London Mathematical Society* s1-10, 4–13. <https://doi.org/10.1112/plms/s1-10.1.4>
- Roisman, I., Tropea, C., 2017. Droplet Breakup, Coalescence, and Wall Impact, in: Michaelides, E.E., Crowe, C.T., Schwarzkopf, J.D. (Eds.), *Multiphase Flow Handbook*. CRC Press.
- Ruzicka, M.C., 2008. On dimensionless numbers. *Chemical Engineering Research and Design* 86, 835–868. <https://doi.org/10.1016/j.cherd.2008.03.007>
- Sadek, C., Pauchard, L., Schuck, P., Fallourd, Y., Pradeau, N., Le Floch-Fouéré, C., Jeantet, R., 2015. Mechanical properties of milk protein skin layers after drying: Understanding the mechanisms of particle formation from whey protein isolate and native phosphocaseinate. *Food Hydrocolloids* 48, 8–16. <https://doi.org/10.1016/j.foodhyd.2015.01.014>
- Salager, J.-L., Choplin, L., 2008. Mousses - Formation, formulation et propriétés. *Techniques de L'ingénieur* 1, 19.
- Schramm, L.L., 2014. Emulsions, Foams, Suspensions, and Aerosols, Second edition. ed. Wiley-VCH.
- Stegeman, Y.W., Van De Vosse, F.N., Meijer, H.E.H., 2008. On the Applicability of the Grace Curve in Practical Mixing Operations. *The Canadian Journal of Chemical Engineering* 80, 1–6. <https://doi.org/10.1002/cjce.5450800414>
- Stevenson, P. (Ed.), 2012. *Foam Engineering Fundamentals and Applications*. John Wiley & Sons, Ltd, Chichester, UK. <https://doi.org/10.1002/9781119954620.fmatter>
- Stone, H.A., 1994. Dynamics of Drop Deformation and Breakup in Viscous Fluids. *Annu. Rev. Fluid Mech.* 26, 65–102. <https://doi.org/10.1146/annurev.fl.26.010194.000433>
- Stone, H.A., Stroock, A.D., Ajdari, A., 2004. Engineering flows in small devices. *Annual Review of Fluid Mechanics* 36, 381–411. <https://doi.org/10.1146/annurev.fluid.36.050802.122124>
- Taylor, G.I., 1934. The Formation of Emulsions in Definable Fields of Flow. *Proceedings of the Royal Society A: Mathematical, Physical and Engineering Sciences* 146, 501–523. <https://doi.org/10.1098/rspa.1934.0169>
- Tsamopoulos, J., Dimakopoulos, Y., Chatzidai, N., Karapetsas, G., Pavlidis, M., 2008. Steady bubble rise and deformation in Newtonian and viscoplastic fluids and conditions for bubble entrapment. *Journal of Fluid Mechanics* 601, 123–164. <https://doi.org/10.1017/S0022112008000517>
- Utada, A.S., Fernandez-Nieves, A., Gordillo, J.M., Weitz, D.A., 2008. Absolute Instability of a Liquid Jet in a Coflowing Stream. *Phys. Rev. Lett.* 100, 014502. <https://doi.org/10.1103/PhysRevLett.100.014502>
- Utada, A.S., Fernandez-Nieves, A., Stone, H.A., Weitz, D.A., 2007. Dripping to Jetting Transitions in Coflowing Liquid Streams. *Phys. Rev. Lett.* 99, 094502. <https://doi.org/10.1103/PhysRevLett.99.094502>
- Van Hoeve, W., 2011. Fluid dynamics at a pinch : droplet and bubble formation in microfluidic devices (Thesis). University of Twente.

- Vial, C., Djelveh, G., 2013. Foisonnement des émulsions alimentaires, in: Legrand, J. (Ed.), *Emulsions alimentaires et foisonnement*. Lavoisier, Paris, France.
- Walstra, P., 2003. *Physical chemistry of foods*, Food science and technology. Marcel Dekker, New York, NY.
- Weaire, D., Drenckhan, W., 2008. Structure and dynamics of confined foams: A review of recent progress. *Advances in Colloid and Interface Science* 137, 20–26. <https://doi.org/10.1016/j.cis.2007.04.001>
- Weaire, D.L., Hutzler, S., 1999. *The physics of foams*. Clarendon Press, Oxford.
- Wyatt, N.B., Gunther, C.M., Liberatore, M.W., 2011. Increasing viscosity in entangled polyelectrolyte solutions by the addition of salt. *Polymer* 52, 2437–2444. <https://doi.org/10.1016/j.polymer.2011.03.053>

Nomenclature

| | |
|------------------------------|---|
| <i>Latin symbols</i> | |
| a | Transition parameter |
| B | Largest radial dimension of a bubble |
| d | Diameter at a given pressure |
| d_{eq} | Equivalent diameter of a sphere |
| d_{32} | Sauter diameter |
| D_{10} | 10 percent of the particles are below this value |
| D_{50} | 50 percent of the particles are below this value |
| D_{90} | 90 percent of the particles are below this value |
| D_h | Hydraulic diameter |
| L | Largest axial dimension of a bubble |
| m | parameter linked to the slope of pseudoplastic region |
| P | Pressure |
| Q | Flowrate |
| U | Superficial velocity |
| V_b | Volume of a bubble |
| <i>Devices</i> | |
| CX600 | Cross-shaped channels with hydraulic diameter of 600 μm |
| CX-E-600 | Cross-shaped channels with hydraulic diameter of 600 μm and an integrated expansion of 1000 μm hydraulic diameter |
| <i>Greek symbols</i> | |
| $\dot{\gamma}_{app}$ | Shear rate at the scale of the process |
| λ | Characteristic Relaxation time |
| μ | Viscosity |
| μ_1 | 1 st Newtonian plateau viscosity |
| μ_2 | 2 nd Newtonian plateau viscosity |
| α | Void fraction |
| ρ | Density |
| σ | Surface tension |
| ΔP | Pressure loss |
| Γ | Bubble aspect ratio |
| φ | Viscosity ratio |
| <i>Subscripts</i> | |
| 0 | At atmospheric pressure |
| G | Gas |
| L | Liquid |
| m | Mass |
| v | Volumetric |
| <i>Dimensionless numbers</i> | |
| Ca_{bubble} | Capillary number of the bubble |
| Ca | Capillary number |
| Re | Reynolds number |
| Oh | Ohnesorge number |
| We | Weber number |

Supplementary material 1

Deformation of gas-liquid interfaces in a non-Newtonian fluid at high throughputs inside a microfluidic device and effect of an expansion on bubble breakup mechanisms

Julian Sepulveda¹, Agnès Montillet², Dominique Della Valle², Catherine Loisel^{2,3}, Alain Riaublanc⁴

¹ LUNAM, Université de Nantes, CNRS, GEPEA, UMR6144, Saint-Nazaire (France).

²ONIRIS, Nantes (France)

³ ONIRIS, GEPEA, UMR CNRS 6144, Nantes (France)

⁴ UR1268 Biopolymères, Interactions, Assemblages, INRA, Nantes (France)

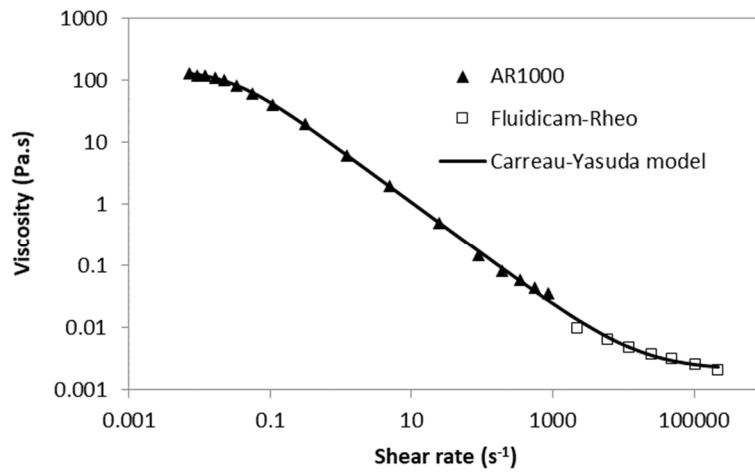


Fig. 1 Solution viscosity data from AR1000 Rheometer and Fluidicam^{RHEO}, and Carreau-Yasuda model using the parameters from table 1 found in the manuscript

Supplementary material 2

Deformation of gas-liquid interfaces in a non-Newtonian fluid at high throughputs inside a microfluidic device and effect of an expansion on bubble breakup mechanisms

Julian Sepulveda¹, Agnès Montillet², Dominique Della Valle², Catherine Loisel^{2,3}, Alain Riaublanc⁴

¹ LUNAM, Université de Nantes, CNRS, GEPEA, UMR6144, Saint-Nazaire (France).

² ONIRIS, Nantes (France)

³ ONIRIS, GEPEA, UMR CNRS 6144, Nantes (France)

⁴ UR1268 Biopolymères, Interactions, Assemblages, INRA, Nantes (France)

Table 2 Experimental conditions inside the microchannel 600 x 600 μm^2

| <i>Device</i> | Q_{vL} | Q_{mG} | p_{abs} | U_G | U_L | $\alpha (p)$ | $\dot{\gamma}_{app}$ | μ_L | μ_F | Ca_L | Re_L | We_L | ΔP | φ |
|---------------|----------------------|----------------------|-----------|----------------------|----------------------|--------------|----------------------|-----------------------|-----------------------|--------|--------|--------|------------|-----------------------|
| (-) | (L h ⁻¹) | (g h ⁻¹) | (Pa) | (m s ⁻¹) | (m s ⁻¹) | (-) | (s ⁻¹) | (Pa.s) | (Pa.s) | (-) | (-) | (-) | (Pa) | (-) |
| CX600 | 11 | 21.6 | 484325 | 2.97 | 8.46 | 0.260 | 1.36×10 ⁵ | 2.40×10 ⁻³ | 3.34×10 ⁻³ | 0.44 | 2058 | 907 | 153000 | 7.29×10 ⁻³ |
| CX600 | 13.7 | 26.5 | 566325 | 3.12 | 10.56 | 0.228 | 1.62×10 ⁵ | 2.35×10 ⁻³ | 3.11×10 ⁻³ | 0.54 | 2617 | 1413 | 197000 | 7.43×10 ⁻³ |
| CX600 | 16.4 | 31 | 653325 | 3.16 | 12.66 | 0.200 | 1.88×10 ⁵ | 2.32×10 ⁻³ | 2.95×10 ⁻³ | 0.64 | 3180 | 2030 | 234000 | 7.53×10 ⁻³ |
| CX600 | 19 | 36.4 | 746325 | 3.25 | 14.75 | 0.180 | 2.13×10 ⁵ | 2.30×10 ⁻³ | 2.84×10 ⁻³ | 0.74 | 3747 | 2759 | 290000 | 7.61×10 ⁻³ |
| CX-E-600 | 11 | 21.6 | 733325 | 1.95 | 8.46 | 0.187 | 1.23×10 ⁵ | 2.42×10 ⁻³ | 3.02×10 ⁻³ | 0.45 | 2036 | 907 | 382000 | 7.21×10 ⁻³ |
| CX-E-600 | 3 | 5 | 333325 | 0.99 | 2.17 | 0.314 | 3.75×10 ⁴ | 3.03×10 ⁻³ | 4.65×10 ⁻³ | 0.14 | 418 | 60 | 112000 | 5.77×10 ⁻³ |

Supplementary material 3

Deformation of gas-liquid interfaces in a non-Newtonian fluid at high throughputs inside a microfluidic device and effect of an expansion on bubble breakup mechanisms

Julian Sepulveda¹, Agnès Montillet², Dominique Della Valle², Catherine Loisel^{2,3}, Alain Riaublanc⁴

¹ LUNAM, Université de Nantes, CNRS, GEPEA, UMR6144, Saint-Nazaire (France).

² ONIRIS, Nantes (France)

³ ONIRIS, GEPEA, UMR CNRS 6144, Nantes (France)

⁴ UR1268 Biopolymères, Interactions, Assemblages, INRA, Nantes (France)

Table 3 Experimental conditions inside the Expansion

| <i>Device</i> | Q_{VL} | Q_{mG} | U_G | U_L | $\alpha (p)$ | $\dot{\gamma}_{app}$ | μ_L | μ_F | Ca_L | Re_L | φ |
|---------------|----------------------|----------------------|----------------------|----------------------|--------------|----------------------|-----------------------|-----------------------|--------|--------|-----------------------|
| (-) | (L h ⁻¹) | (g h ⁻¹) | (m s ⁻¹) | (m s ⁻¹) | (-) | (s ⁻¹) | (Pa.s) | (Pa.s) | (-) | (-) | (-) |
| CX-E-600 | 11 | 21.6 | 0.7021 | 3.046 | 0.1873 | 2.67×10 ⁴ | 3.34×10 ⁻³ | 4.17×10 ⁻³ | 0.22 | 885 | 5.22×10 ⁻³ |
| CX-E-600 | 3 | 5 | 0.3576 | 0.780 | 0.3142 | 8.10×10 ³ | 5.56×10 ⁻³ | 8.55×10 ⁻³ | 0.09 | 136 | 3.14×10 ⁻³ |